Journal of Electroanalytical Chemistry 920 (2022) 116645

Contents lists available at ScienceDirect

Journal of Electroanalytical Chemistry

journal homepage: www.elsevier.com/locate/jelechem

Molten salt synthesis of nitrogen-doped hierarchical porous carbon from plantain peels for high-performance supercapacitor

Nashiru Mahadeen Nanzumani [a], Frank Ofori Agyemang [a,*], Kwadwo Mensah-Darkwa [a], Eugene Sefa Appiah [a], Emmanuel Kwesi Arthur [a], Emmanuel Gikunoo [a], Bennetta Koomson [a], Amol R. Jadhav [b], Akeem Raji [c]

[a] Department of Materials Engineering, College of Engineering, Kwame Nkrumah University of Science and Technology, Kumasi, Ghana
[b] Center for Integrated Nanostructure Physics (CINAP), Institute for Basic Science (IBS), Sungkyunkwan University, Suwon 16419, South Korea
[c] Department of Creative Convergence Engineering, Hanbat National University, Daejon 34158, South Korea

ARTICLE INFO

Keywords:
Hierarchical porous carbon
N-doped
Molten salt
Supercapacitor
Plantain peels

ABSTRACT

This work employs a non-corrosive and non-toxic molten salt combination of NaCl and KCl as an activation agent in an air environment to synthesize nitrogen-doped hierarchical porous carbon from plantain peels at 800 °C for supercapacitor application. Due to the synergistic effect of nitrogen doping, the synthesized nitrogen-doped activated unripe porous carbon (AUPN) has a hierarchical (micro-meso-macropores) porous structure and a high surface area of 959 m^2/g, providing sufficient active sites for charge storage, rapid electrolyte and ionic mobility. X-ray diffraction and Raman spectroscopy analysis revealed the formation of a carbon product with a limited degree of graphitization and the crystallite size (L_a), which is valuable for evaluating the defects caused by nitrogen doping. In a three-electrode cell with a 6 M KOH electrolyte, AUPN recorded a specific capacitance of 550 F/g at 1 A/g. After 1000 cycles, capacitance retention was 99% at 4 A/g. Compared to other reported porous carbon materials, the overall electrochemical performance of AUPN is superior. This is due to the abundant nitrogen-doping, which introduces pseudocapacitance and increases the surface wettability of the porous carbon, resulting in a decrease in ionic-transport resistance.

These findings indicate that this green and scalable technique is a potential synthesis method for producing porous carbon materials for energy storage applications.

1. Introduction

To meet modern society's energy concerns, clean, sustainable energy, as well as effective energy storage technologies, are necessary [1,2]. Energy storage technologies have become of paramount importance because of the intermittent nature of different renewable energy sources. Hence, investment in energy storage technologies such as supercapacitors and batteries are advancing. Supercapacitors have played an essential part in the energy storage sector due to their high-power capability, fast charge–discharge rate, and long cycle life [3,4]. Because of its exceptional properties such as tailorable pore structures, excellent electrical conductivity, high active surface areas, and strong thermal/chemical stabilities, porous carbon materials are regarded as the ideal electrode materials for supercapacitors [5]. They are mostly used in portable electronics, electric vehicles, and uninterruptible power supply, among others [6]. The significant difficulty, however, lies in their low specific energy. As a result, there has been an increase in research interest in improving the performance of supercapacitors using various approaches, such as using inexpensive electrode materials, modifying the textural properties of carbons, using various electrolytes, and developing novel, highly efficient energy storage devices [7].

Porous carbon (PC) for energy storage has been widely researched [8–11]. On the other hand, electrodes used in energy storage systems are mostly made from non-renewable resources such as coal, peat petroleum coke, and so on [7,12]. Biomass is sustainable and high in carbon content, and it has attracted much interest in recent years as a source of porous carbon for a variety of uses. Researchers have looked at using different biomass carbon precursors for the production of porous carbon via a variety of synthesis methods and using them as electrodes in energy storage applications [13–15]. Various biomass precursors, such as ginger [16], wheat straw [17], lotus leaf [18], kitchen waste residue [19], onion [5], clover [1], bamboo shells [20], human hair [13,21], and albizia flowers [15], have been used

* Corresponding author.
E-mail address: foagyemang@knust.edu.gh (F.O. Agyemang).

https://doi.org/10.1016/j.jelechem.2022.116645
Received 2 April 2022; Received in revised form 4 July 2022; Accepted 18 July 2022
Available online 21 July 2022

to prepare hierarchical porous carbon for supercapacitor electrode material. Compared to non-renewable carbon resources, biomass can be a sustainable resource for producing hierarchical porous carbons for energy applications. Chemical activation techniques typically utilize corrosive and toxic chemicals such as KOH and $ZnCl_2$ to produce porous carbon materials. The use of these poisonous and corrosive activation chemicals, on the other hand, renders the production process unsustainable, particularly for industrial applications. Furthermore, the end products of chemical activation with KOH include a lot of micropores, a few mesopores, and no macropores. This slows the diffusion rate and reduces the electrode material's overall performance. Furthermore, inert atmospheres (such as Ar and N_2) are the primary processing environment employed during the synthesis of porous carbon, which raises production costs and impedes commercial production. In light of these concerns, it is critical to develop a sustainable and cost-effective synthesis technique for producing porous carbon with abundant and interconnected pores (micro, *meso*, macro) to improve the electrode material's diffusion rate and overall performance for supercapacitor applications [1,10]. Arthi et al. [16] produced hierarchical porous thin carbon nanosheets from ginger as carbon precursor, employing a non-toxic NaCl/KCl salt combination as activation media. At 0.3 A/g, the porous carbon electrode has a high specific capacitance of 456 F/g. It also has high cyclic stability of 95% after 10,000 cycles [16]. Wang et al. [1] also synthesized highly porous carbon sheets from fresh clover stem in an air atmosphere using a simple potassium chloride salt-etching technique. When used as supercapacitor electrodes, they exhibit a high specific capacitance of 436 F/g at 1 A/g and an excellent rate capacity with capacitance remaining 290 F/g at 50 A/g [1]. Results obtained from this study using a molten salt medium and an air atmosphere are similar to results reported in literature that employ this green and scalable technique [1,12,19,22].

In this regard, plantain peels are an underused renewable, low-cost, and environmentally friendly resource composed mostly of functional groups such as amino acids, hydroxyl etc. Plantain peels may be a severe disposal issue in locations where plantains are grown and consumed in large quantities. If this resource can be transformed into carbon materials for energy storage applications, it will give a value-added product for different uses while also assisting with waste management. It is composed of cellulose, hemicellulose, hydrocarbons, and chlorophyll pigment. Porous carbon derived from plantain peels has been investigated for a variety of applications including transesterification [23], antimicrobial activity [24], adsorption [25] and heterogeneous catalysis [26]. As far as we know, no previous research has investigated the conversion of plantain peels using the molten salt technique for supercapacitor application.

Herein, the current study made use of a green synthesis approach. The use of molten salt activation in an air environment resulted in a significant improvement in overall electrochemical performance. Plantain peels were used as the carbon precursor, ammonium chloride (NH_4Cl) as the N source, and a low cost and a non-toxic salt mixture of potassium chloride (KCl) and sodium chloride (NaCl) were used as dual function agents for activation of the precursor to achieve high specific surface area by building hierarchical porous structures during one-step carbonization and protection of the generated porous carbon structure from being destroyed by air at high temperatures. As a result, the as-obtained porous carbon has an interconnected porous carbon structure with a large surface area of 959 m^2/g, which can provide plentiful storage sites and promote charge and mass transmission [9,27]. Furthermore, the incorporation of heteroatom doping (N = 7.98%) in the porous carbon structure improves electrochemical performance by increasing electrochemical reactivity and electronic conductivity, reducing ion diffusion and charge transfer resistance, and improving capacitive performance [13,28]. The developed hierarchical porous carbon has impressive structural properties that make it appropriate for supercapacitor applications. As a result, the hierarchical porous carbon exhibits a high specific capacitance of 550 F/g at 1 A/g in a three-electrode system as a supercapacitor electrode. After 1000 cycles at 4 A/g, the material retains 99% of its capacitance, indicating its remarkable cyclability and rate capacity. The synthesized hierarchical porous carbon exhibits superior electrochemical performance in terms of specific capacitance and cycle stability. When compared to previously reported biomass produced porous carbons, the obtained overall electrochemical performance is better [1,2,14,29,30].

2. Materials and methods

2.1. Materials

Plantain peels were obtained from a canteen around Ayeduase, Kumasi, Ghana. Sigma Aldrich provided ammonium chloride (NH_4Cl, >99.5%), hydrochloric acid (HCl, >30%), potassium hydroxide (KOH, >85%), potassium chloride (KCl, >99%), polyvinyl alcohol (PVA, 99+% hydrolysed) and sodium chloride (NaCl, 100%). Throughout the experiment, deionized water (DI) was utilized.

2.2. Synthesis of activated porous carbon

The synthesis of porous carbon was based on the molten salt technique proposed by [10]. Ripe and unripe plantain peels (RPP and UPP) were collected from a canteen around Ayeduase. The samples were thoroughly washed and dried at 105 °C for 24 h using deionized water. The dried samples were crushed using a ceramic mortar and pestle and sieved to 125 μm particle size. NaCl/KCl salt combination (1:1) was submerged in 200 mL deionized water and slowly heated and agitated. Using a carbon precursor: NaCl/KCl ratio of 1:3, RPP and UPP powders were mixed with the salt, stirred overnight, and then dried at 105 °C for 6 h. Finally, the salt-treated-RPP and salt-treated UPP were activated. The activation was carried out as follows: The salt-treated-RPP and salt-treated UPP were put in separate 100 mL porcelain crucibles with a lid and placed in a furnace. Using a heating rate of 10 °C/min, the samples were heated at 800 °C in an air environment for 3 h. After allowing the muffle furnace to cool to ambient temperature, the resultant products were washed multiple times with 1 M HCl solution and distilled water until a pH of 7.0 was obtained. The samples were dried at 105 °C for 12 h in an oven. The two different porous carbon produced were labeled as activated ripe porous carbon (ARPP) and activated unripe porous carbon (AUPP).

2.3. Synthesis of N-doped porous carbon

Nitrogen-doped porous carbon was produced using ammonium chloride (NH_4Cl) as nitrogen source. First, ammonium chloride was thoroughly mixed with RPP and NaCl/KCl using a mass ratio of RPP: NaCl/KCl: NH_4Cl = 1:3:1, then the obtained mixture was directly treated at 800 °C in an air induced atmosphere for 3 h. The resulting product was then neutralized with 1 M HCl and DI water before drying for 12 h at 105 °C. ARPN was employed as a marker for the produced *N*-doped porous carbon. The same method was used with UPP, and the resulting product was labeled as AUPN. The carbon yields of the samples are summarized in Table S1.

2.4. Characterization

FESEM, JEOL-7600F was used to analyse the morphology of the produced porous carbons. The crystal structure was determined using an X-ray diffractometer (Bruker AXS D8 Advance) outfitted with Cu-K_α (λ = 1.5418 Å). The Raman spectra were recorded using a Renishaw inVia Raman spectrometer with a laser excitation energy of 532 nm. FTIR spectra were acquired using a Bruker R 200-L. Micromeritics ASAP 2020 analyzer is used to determine the surface area (Bru-

nauer–Emmett–Teller (BET)) and the pore size distribution (Barrett-Joyner-Halenda (BJH)) at 77 K. Vario EL III was used to determine the elemental composition of the samples.

2.5. Electrochemical analysis

The working electrodes for three-electrode electrochemical experiments were prepared by combining the as-prepared porous carbons (90%) with PVA (10%) and adding a few drops of water to produce a slurry. The slurry was then coated onto carbon foam and oven-dried overnight at 60 °C. Each electrode has a coated electrode area of 1 cm^2 and a mass loading of ~3 mg. Aqueous KOH (6 M) was used as an electrolyte, and Corrtest Electrochemical Workstation (Wuhan, China) was used for the electrochemical analysis. Ag/AgCl and graphite rod were used as reference and counter electrodes, respectively. At various scan rates and current densities, cyclic voltammetry (CV) and galvanostatic charging-discharging (GCD) studies were carried out using a potential window ranging from 1.2 to 0.2 V (vs Ag/AgCl). With an amplitude of 5 mV, Electrochemical Impedance Spectroscopy (EIS) was performed within a frequency range of 0.01 Hz to 100 kHz.

The discharge curves were used to compute the specific capacitance of each electrode in a three-electrode system using the equation:

$$C = \frac{I\Delta t}{m\Delta V} \tag{1}$$

where I(A) is the discharge current, $\Delta t(s)$ the discharging time, m(g) the mass of the electro-active material and ΔV is the potential change within the discharge time Δt.

3. Results and discussion

Elemental analysis is used to determine the elemental composition of the samples and the findings are displayed in the Supplementary Information (SI) Table S1. C (43.89%), N (0.86%), H (8.55%) and S (3.37%) are found in the unripe plantain peel precursor, whereas C (40.98%), N (0.57%), H (8.19%) and S (2.55%) are found in the ripe plantain peel precursor. The Sulphur element is reduced to zero after high-temperature molten salt activation of the doped samples (ARPN and AUPN), while the nitrogen and carbon content increases. These findings show that nitrogen can be effectively doped into carbon through the molten salt activation process. When compared with samples generated without doping (ARPP and AUPP), the carbon and nitrogen content of the raw samples (RPP and UPP) is much lower, showing that the activation process promotes decomposition [31]. The initial feedstock composition is an important factor that affects the overall performance of the synthesized porous carbons. Plantain peels were chosen as the primary carbon source because they are a rich biomass resource with several carboxyl and hydroxyl groups that play essential roles in energy storage applications. Because of its large fraction of amino functionalities, ammonium chloride (NH_4Cl) was also used to increase the nitrogen content, resulting in increased pseudocapacitance. A proposed process for the synthesis of the hierarchical porous carbons is described. In the entire process, the KCl/NaCl salt combination serves as a protective agent, preventing the decomposition of the carbon structure and nitrogen element by a sealing action that reduces the contact between the carbon structure and O_2 [4,19,32].

Fig. 1 depicts the schematic representation of the synthesis process in molten salt under an air environment. Carbonization of the biomass precursor at high temperatures would result in a continuous change from sp^3 C-X (X: e.g., C, H, O) bonds to aromatic sp^2 C—C, which would form the skeleton of the desired carbon structure and graphite microcrystals. Reduced sp^3 C-X might result in the release of the graphite microcrystals because sp^3 C-X assisted in crosslinking and limited the graphite microcrystals. The salt crystals and particles of various sizes were removed after washing with deionized water, leaving an interconnected pore structure. The traces of O_2 would also etch the carbon skeleton, forming more pores and promoting the formation of an interconnected porous structure [19,33].

The two raw bio-waste samples (UPP and RPP), their hierarchically activated (AUPP and ARPP) and nitrogen-doped porous carbons (AUPN and ARPN) were analyzed using FTIR. From the FTIR spectra in Fig. S1, UPP and RPP showed numerous bands. The C — H stretching is shown by the peak at about 3000 cm^{-1}. The aliphatic C — N stretch is approximately around 1020 cm^{-1} – 1220 cm^{-1}, while the aromatic C — N stretch is around 1250 cm^{-1} – 1360 cm^{-1}. Furthermore, the peaks between 1665 cm^{-1} – 1760 cm^{-1} suggest carboxylic acids (COOH). C=C stretch may be found between 1600 cm^{-1} – 1680 cm^{-1} [12]. The C — H bending is seen by the absorption band between 1650 and 2000 cm^{-1}. The O — H stretch is recognized as a band between 2500 and 3500 cm^{-1}. Most of the functional groups disappeared as a result of carbonization and activation. This is because decomposition and dehydration occur at high temperatures, resulting in the disappearance of the peaks for the hierarchical porous carbons (AUPP and ARPP) [28]. After doping with NH_4Cl, the appearance of a weak absorption peak around 1020 cm^{-1} – 1250 cm^{-1} indicates C—N stretch and the weak absorption peak around 1500 cm^{-1} – 1550 cm^{-1} is ascribed to N—O stretching. The appearance of these two peaks for the *N*-doped samples (AUPN and ARPN) confirms that the synthesized porous carbon has been successfully doped with nitrogen [34].

Fig. 2(a) shows the X-ray diffraction (XRD) peaks for the samples AUPP, ARPP, ARPN and AUPN. Two broad peaks are observed around 23°–25° corresponding to the (0 0 2) plane and 44°–45° range corresponding to the (1 0 0) plane of graphite, indicating the formation of the carbon product with a limited degree of graphitization [10,30]. The phase angle for the (0 0 2) plane is 25.1°, 23.2°, 24.7° and 23.1° for AUPP, ARPP, ARPN and AUPN, respectively. Furthermore, the high peak intensity in the low-angle region indicates the formation of a highly developed interconnected porous structure with low crystallization [4,35]. Thus, charges can be stored in the developed interconnected pores due to the presence of random graphene layers in amorphous carbon [12,29]. The decreased intensity of the (0 0 2) peak, especially for the nitrogen-doped carbons (ARPN and AUPN), indicates an increase in structural disorder due to gas escape from NH_4Cl during high-temperature activation [11,17].

Raman spectroscopy was used to further analyze the degree of graphitization, as seen in Fig. 2(b). The disordered (D) and ordered graphitic (G) carbon features are shown by the peaks at 1348 cm^{-1} and 1590 cm^{-1}, respectively. The D band represents the disorder in amorphous and nanocrystalline carbon due to defects or tiny crystallite sizes. The first-order Raman scattering relates the G band to the graphitic structure [36–38]. The D band's intensity ratio to the G band's intensity (I_D/I_G) indicates the degree of graphitization. AUPP, ARPP, ARPN, and AUPN have I_D/I_G values of 0.91, 0.98, 1.05, and 1.12, respectively. With the addition of the nitrogen dopant, the degree of disorder and defects rises, suggesting that pore creation and nitrogen doping increase the disorder and defects in the materials. Thus, a higher degree of graphitization can improve electrical conductivity while also increasing specific capacitance [39–41]. The crystallite size (L_a) of the synthesized porous carbon materials was calculated using equation (2):

$$L_a = \frac{4.4}{(I_D/I_G)} \tag{2}$$

where L_a is the crystallite size of the synthesized porous carbon materials and I_D and I_G are the D and G peaks, respectively.

L_a is useful for studying the defects generated by nitrogen doping since fewer defects imply a higher La and more defects imply a lower L_a. With the addition of nitrogen dopant, smaller L_a with more defects signifies a drop in crystallite size [37,42,43]. Table S2 displays the I_D/I_G values and average crystallite sizes of the porous carbon samples.

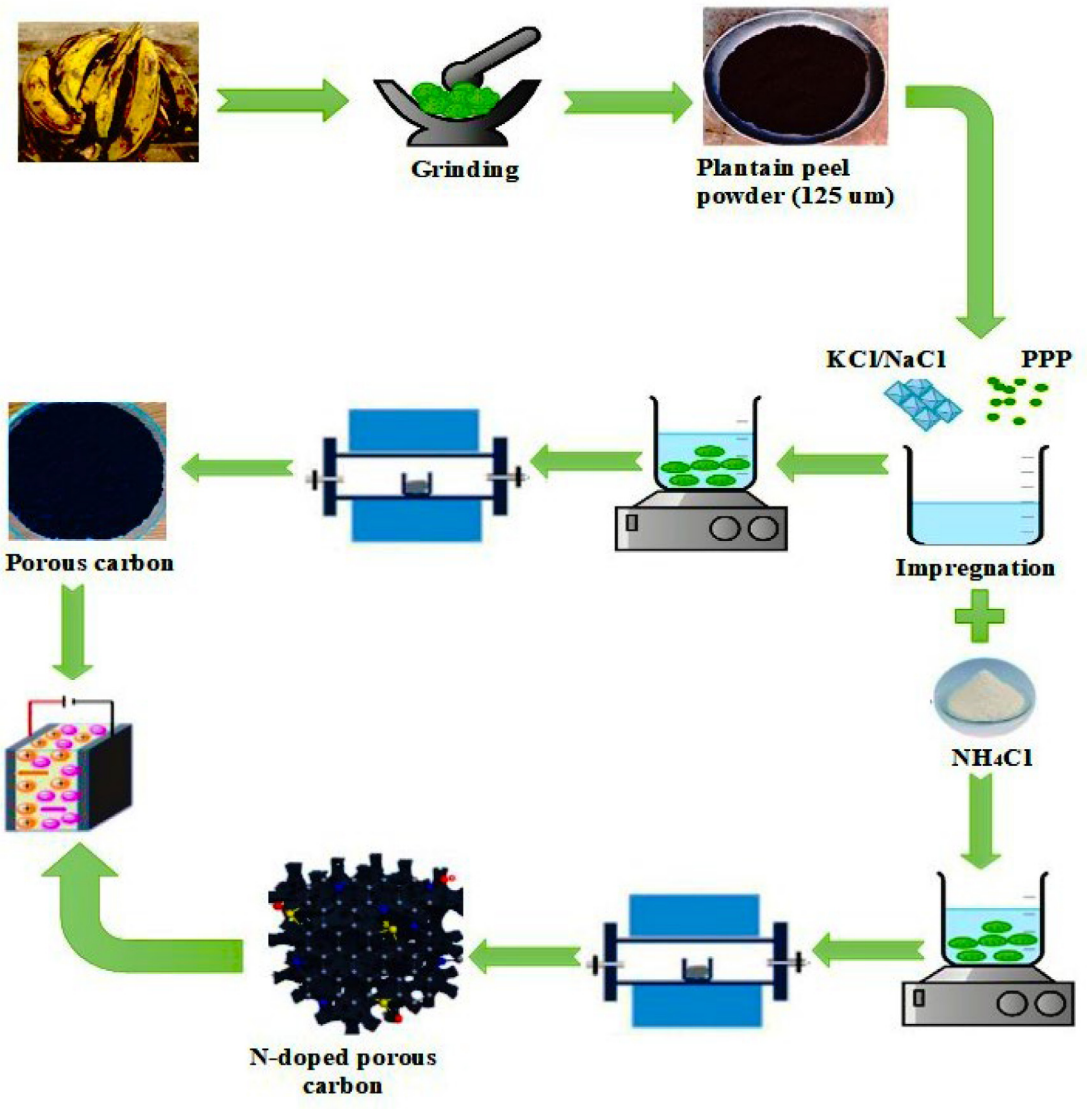

Fig. 1. Schematic illustration of the synthesis process of porous carbon and *N*-doped porous carbon in air.

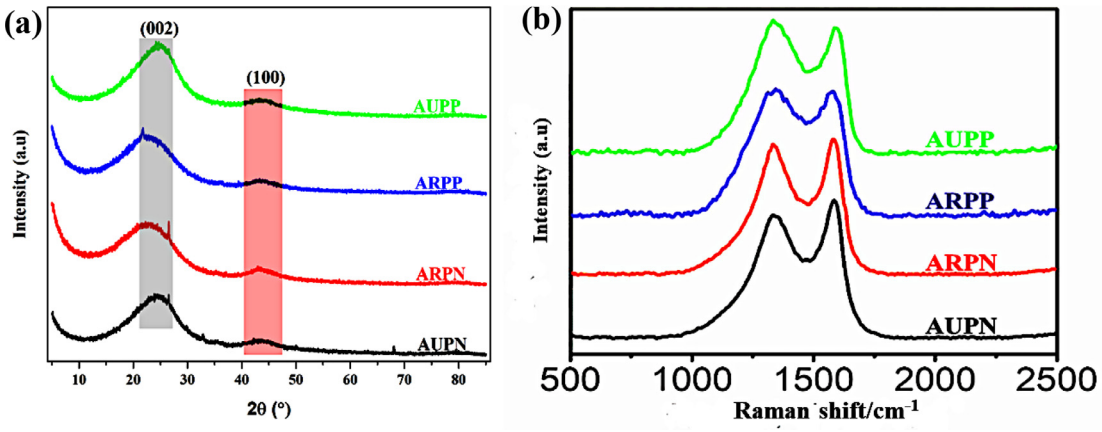

Fig. 2. (a) XRD patterns and (b) Raman spectra of AUPP, ARPP, ARPN and AUPN.

The nitrogen adsorption/desorption isotherms of AUPN, ARPN, ARPP, and AUPP are shown in Fig. 3(a). All four samples correspond to the I/IV-type adsorption/desorption isotherm, indicating the presence of many micropores and mesopores [44]. Within the low P/P_0

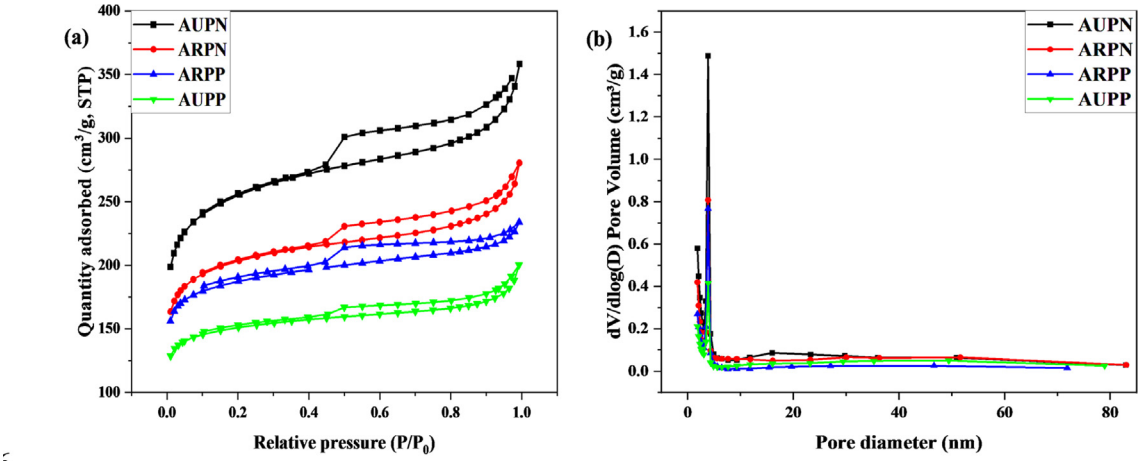

Fig. 3. (a) Nitrogen adsorption/desorption isotherms and (b) BJH pore size distribution of AUPN, ARPN, ARPP and AUPP.

region, there is a rapid upward trend indicating the presence of abundant micropores within AUPN, giving rise to the obvious higher nitrogen uptake than ARPN, ARPP, and AUPP. Also, around $P/P_0 > 0.4$, a characteristic hysteresis loop is formed, indicating the presence of significant mesopores. Within the high P/P_0 region, a steady rise indicates the presence of mesopores and macropores – these findings support the formation of an interconnected porous structure within the samples [1,10]. The samples' specific surface area (SSA) was determined using Brunauer-Emmett-Teller (BET), and the related pore volume is shown in Table 1.

AUPN has an SSA of 959 m^2/g and a pore volume of 0.53 cm3/g, which is reportedly greater than ARPN (774 m^2/g, 0.41 cm^3/g), ARPP (726 m^2/g, 0.35 cm^3/g), and AUPP (588 m^2/g, 0.29 cm^3/g). The large specific surface area of AUPN is due to NH_4Cl doping, which produces additional defects in the carbon structure after activation. Because of the large specific surface area, suitable electrode/electrolyte interfaces may be provided for ion or charge buildup [45,46]. Fig. 3(b) depicts the BJH pore size distribution of the samples mentioned above, indicating that AUPN has a superior pore distribution in the region of micropores and mesopores. The results indicate that using a molten salt combination (KCl/NaCl) and nitrogen doping (NH_4Cl) to synthesize a hierarchical porous structure based on plantain peels biomass is advantageous. At high carbonization temperature, the emission of various non-carbon and carbon components and the amplification of the burn-off of plantain peels precursor will cause many nearby micropores to collapse or form mesopores and macropores [14,18].

Photographs and FESEM images in Fig. 4 depict plantain peels (ripe and unripe). From Fig. 4(c, d), the plantain peels are composed of well-aligned planar substructures with thin walls that are segregated from one another, allowing molten salt KCl/NaCl to permeate easily. Meanwhile, the thin walls can be exfoliated into carbon sheets by molten salt and trace oxygen in the air [10,16]. The FESEM examination also determined the morphologies of the synthesized hierarchical porous carbons. The FESEM images in Fig. 5 show that the produced porous carbons are very porous. The pores formed are a mix of small and large pores. Some big pores may have been generated during porous carbon synthesis due to the expansion of tiny pores at high temperatures during the activation step [47,48]. The carbon materials used as electrodes must have an interconnected porous network so that ionic diffusion happens quickly during the electron transfer operations [49,50]. Furthermore, the increased surface area of electrode materials gives more sites for electrolyte solution across the electrode/electrolyte interface and aids in creating an electrical double layer [51–53].

Fig. 5(c, d) depicts the AUPN surface as an interconnected and distributed microporous and mesoporous architecture with randomly deposited carbon layers. This morphology might be explained by molten salt activation and doping with KCl/NaCl and NH_4Cl [5,16]. This hierarchical porous structure is responsible for AUPN's superior electrochemical performance compared to other materials. Thus, the network of macropores and mesopores acts as a solution buffering reservoir, reducing diffusion distance and promoting mass movement while also reducing volume change during charge/discharge cycling, providing good cycling performance [10,22]. In contrast, the mesoporous/microporous network enhances the specific surface area by providing abundant adsorption sites for electrolyte ions [54,55]. The ARPN structure in Fig. 5(g, h) is also porous with few variations compared to AUPN. ARPN displays an interconnected mesoporous architecture constructed by numerous randomly distributed agglomerated mesopores. Due to the layer stripping effect of the gas produced by the reaction, which generates pores, NaCl/KCl during the activation phase assists in forming the linked carbon structure. Nitrogen doping induces defects in the carbon network, resulting in a more porous microstructure and more easily accessible active sites [10,20]. The formation of the porous structure might be linked to synergistic actions such as etching, intercalation effect, and the generated NaCl/KCl template, which has the potential to produce a hierarchical morphology. For the electrode material used in supercapacitors, the numerous

Table 1
Textural characteristics of as-synthesized hierarchical porous carbons.

Sample	S_{BET} (m^2/g)	S_{Micro} (m^2/g)	S_{Meso} (m^2/g)	V_{total} (cm^3/g)	V_{Micro} (cm^3/g)	V_{Meso} (cm^3/g)	$D_{average}$ (nm)
AUPN	959	651	307	0.53	0.26	0.27	3.87
ARPN	774	567	207	0.41	0.22	0.19	4.15
ARPP	726	569	157	0.35	0.22	0.13	3.62
AUPP	588	475	113	0.29	0.18	0.11	4.63

S_{BET} = total BET surface area; S_{meso} = mesopore surface area; S_{micro} = micropore surface area; V_{total} = total pore volume; V_{meso} = mesopore volume; and V_{micro} = micropore volume. $D_{average}$ = average pore diameter.

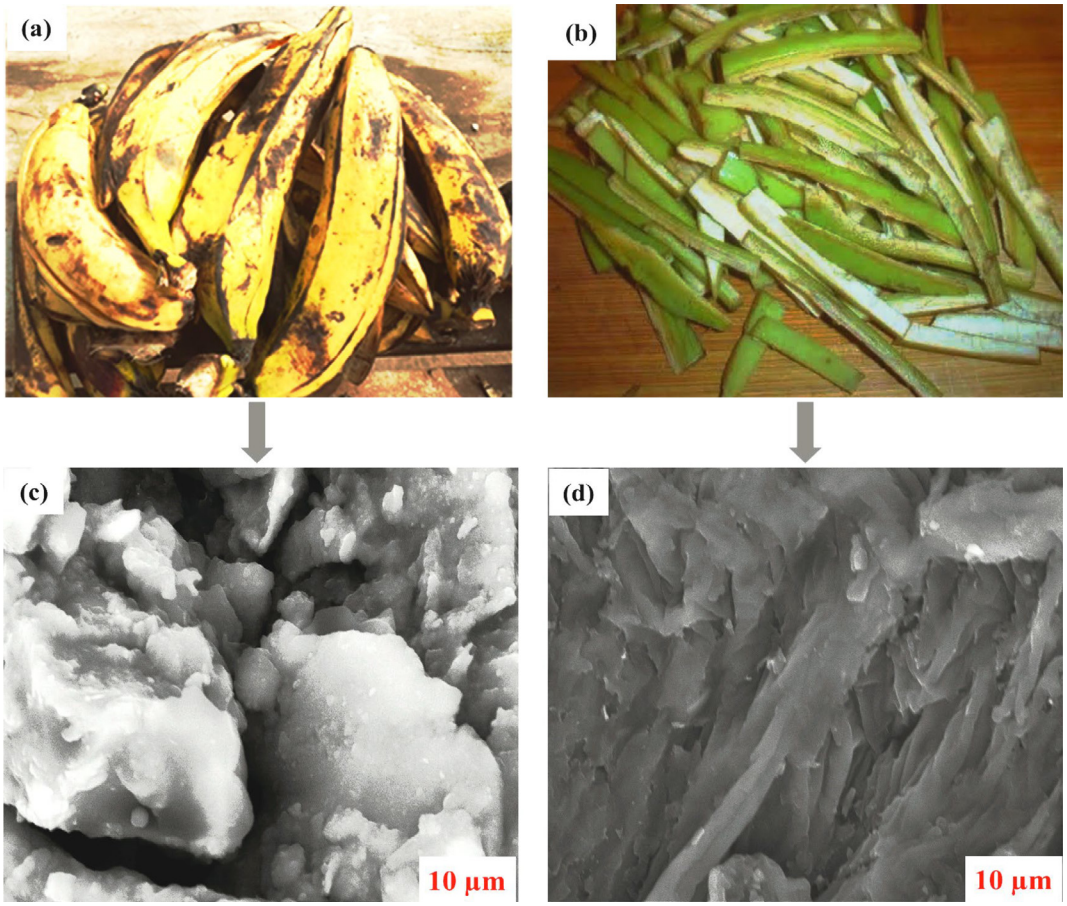

Fig. 4. (a) Photograph of ripe plantain peels, (b) photograph of unripe plantain peels and (c) FESEM image of ripe plantain peels, (d) FESEM image of unripe plantain peels.

micropores and homogenous mesoporous structures are more beneficial for charge storage and electrolyte transfer [28,56].

It can be deduced that; carbon materials can be activated with a molten salt combination (KCl/NaCl) to form unique pore architecture. Activation of AUPP (Fig. 5(a, b)) and ARPP (Fig. 5(e, f)) was accomplished using NaCl/KCl without doping with NH_4Cl. Thus, without doping with NH_4Cl, ARPP and AUPP demonstrate more microporous morphologies. This provides both samples with a less porous structure in a carbon matrix and conforms with their less surface area, as reported above [57]. Furthermore, by accelerating the thermal decomposition of precursors and producing extra defects that serve as charge storage sites, NH_4Cl plays an important role in forming highly developed hierarchical porous structures. As a result, NH_4Cl promotes the formation of many mesopores and macropores [29,58].

The electrochemical performances of the samples in a 6 M KOH aqueous solution were tested using a three-electrode setup. The cyclic voltammetry (CV) curves of all samples are shown in Fig. 6(a) at a scan rate of 10 mV/s from −1.2 to 0.2 V. All samples have a desirable rectangular shape, which indicates that they have good electric double-layer capacitance behavior and high stability in a 6 M KOH electrolyte [8]. ARPN and AUPN show weak humps due to a mix of normal EDLC behavior and limited faradic reaction caused by nitrogen doping. AUPN has the largest area, corresponding to its highest specific capacitance due to better surface area and nitrogen doping, whereas AUPP has the lowest. Fig. 6(b) shows the corresponding GCD curves for all four samples at a current density of 1 A/g. All of the samples are linear and symmetrical, with minor humps, showing that double-layer capacitance has good capacitive behavior with low pseudocapacitance and minimum equivalent series resistance (iR drop) [16,59]. Compared to other samples, AUPN has the longest charge and discharge duration, showing superior capacitive performance. The calculated specific capacitance of AUPN from the GCD curves is 550 F/g at 1 A/g, which is better than the specific capacitances of ARPN (348 F/g), ARPP (180 F/g), and AUPP (175 F/g) at the same current density.

Fig. 7(a, b) and (c, d) depict how the change in scan rate (5–100 mV/s) and current density (1–5 A/g) affect the specific capacitance of AUPP and AUPN, respectively. All of the samples' CV curves are quasi-rectangular in shape [60]. As predicted, the specific capacitance falls as the scan rate increases. Even at a high scan rate of 100 mV/s, there are no sudden changes, indicating excellent capacitive performance. At high scan rates, electrolyte ions do not have enough time to diffuse and utilize all active sites for charge storage [61]. The triangular form is still preserved for all samples at higher current densities, suggesting excellent reversibility during the GCD process. A similar trend is observed in Fig. 8 (a, b)- (c, d) for the ARPP and ARPN samples.

The specific capacitance of all four samples at varied current densities (1–5 A/g) is shown in Fig. 9(b). When current density increases, the specific capacitance drops, which is connected to the rise in diffusion restriction. Electrolyte ions could not easily penetrate into pores at high current densities, resulting in effective ion attachment occurring only at the electrode's surface [10,62]. However, electrolyte ions could quickly move and diffuse into the pores when the current density was reduced. As a result, the capacitance was higher at low current density than at high current density [63–65]. For example, AUPN, ARPN, ARPP, and AUPP specific capacitances were 255 F/g, 117 F/g, 26 F/g, and 15 F/g, respectively, at a current density of 5 A/g.

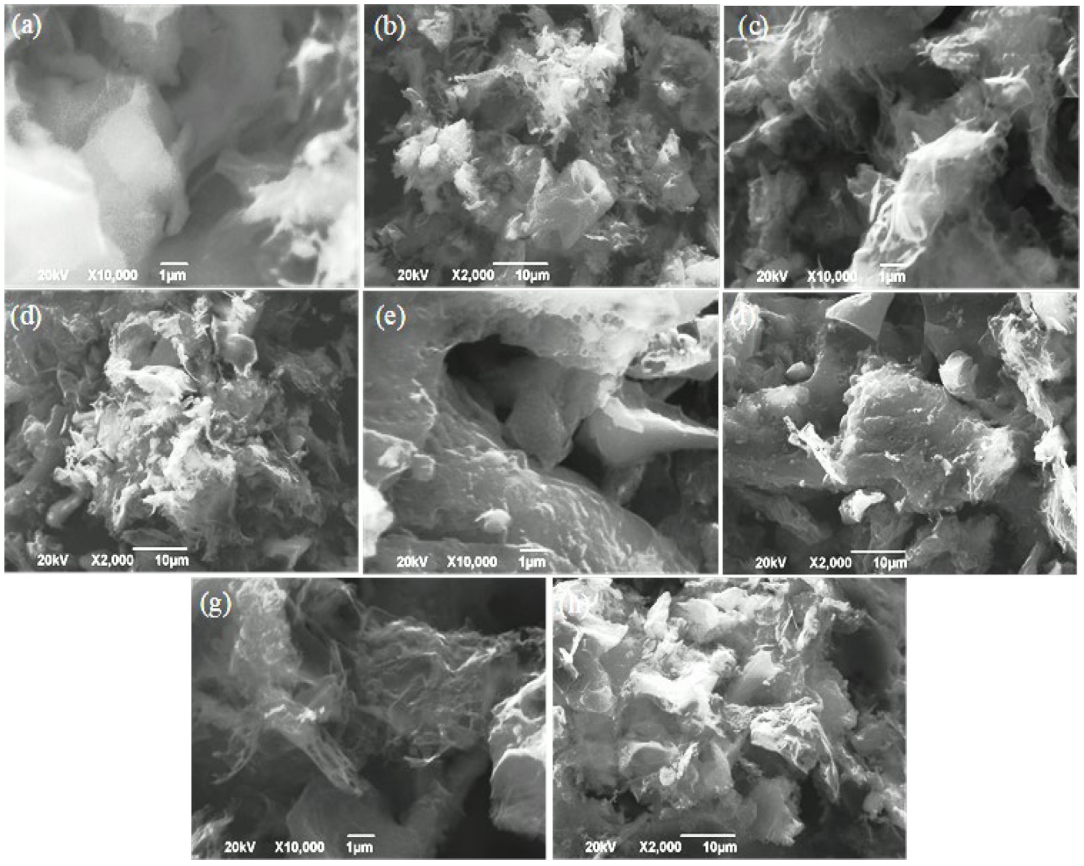

Fig. 5. FESEM images of (a, b) AUPP, (c, d) AUPN, (e, f) ARPP and (g, h) ARPN.

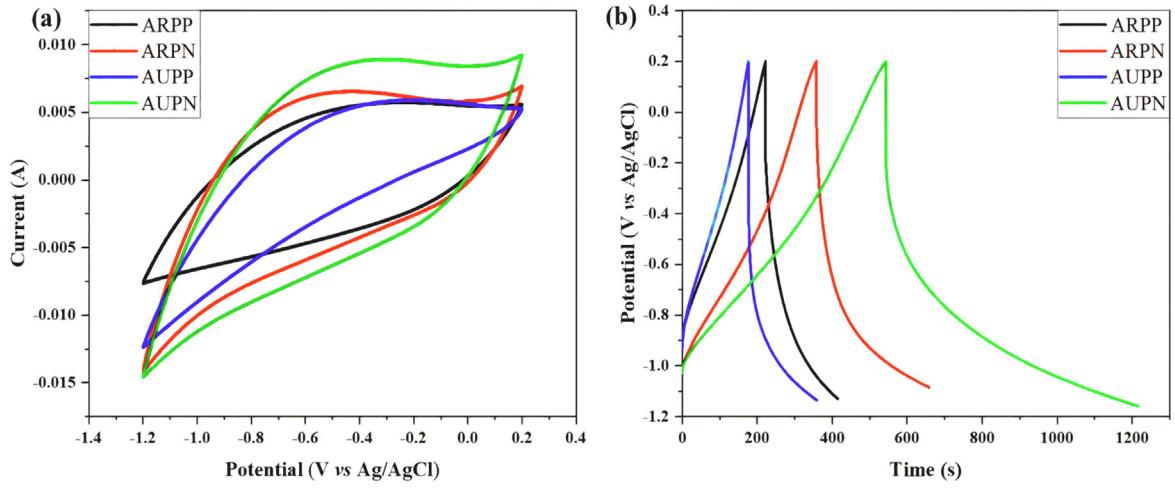

Fig. 6. AUPN, ARPN, ARPP, and AUPP electrochemical performance in a three-electrode system utilizing 6 M KOH aqueous solution (a) CV curves at 10 mV/s and (b) GCD curves at 1 A/g.

The specific capacitance of this doped sample (AUPN) improved more than the other samples, owing to the nitrogen's enhanced conductivity, surface wettability, and charge transfer efficiency [66,67]. Because of the hierarchical pore structure and nitrogen doping impact of the AUPN electrode, AUPN shows a combined characteristic of electrical double-layer capacitance and pseudocapacitance. The capacitance control process for AUPN comprises ion adsorption/desorption and surface redox reactions, demonstrating a combined contribution of diffusion-controlled and capacitance-controlled processes. As a result, the electrode exhibits battery- and supercapacitor-like characteristics [29,37,39]. The contribution of double-layer capacitance and pseudocapacitance highlights the AUPN electrode's rapid electrochemical kinetics and remarkable capacity [19].

EIS analysis was used to examine transport kinetics and the mechanism of electrolyte ion diffusion. The Nyquist plots for AUPN, ARPN, ARPP, and AUPP are shown in Fig. 9(a). The samples display a nearly vertical line along the Z”-axis in the low-frequency region, demonstrating appropriate capacitive behavior and minimal ion diffusion resis-

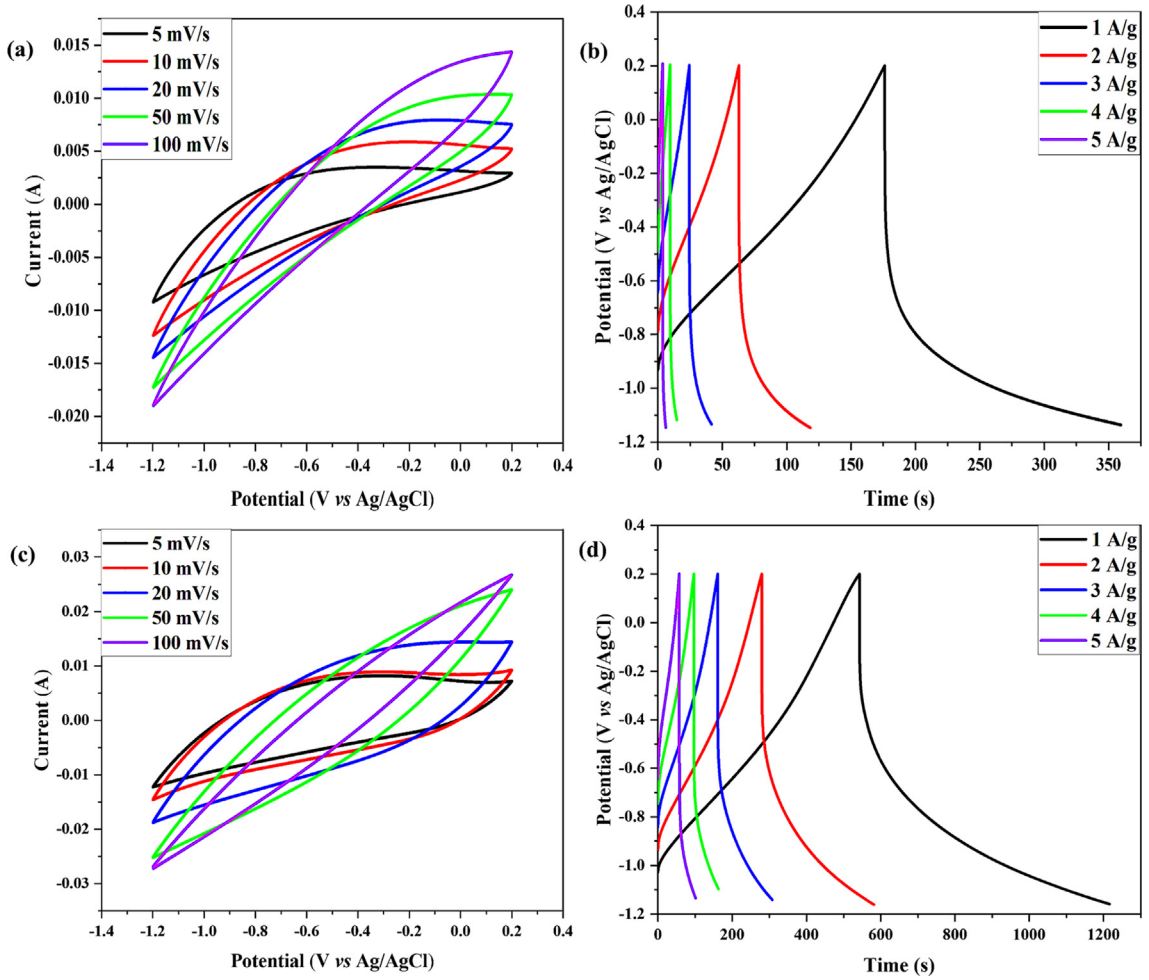

Fig. 7. CV curves at different scan rates and GCD curves at different current densities of AUPP (a,b), CV curves at different scan rates and GCD curves at different current densities of AUPN (c,d).

tance in the electrode materials. Warburg impedance was detected in the medium frequency range, where the electrolyte ion entered into the depth of the micro/mesoporous network of the electrode materials. The charge transfer resistance is responsible for the semi-circular behavior observed at high-frequencies [68]. The inset shows that AUPN has the smallest semicircle in the high-frequency area, meaning that it has superior conductivity and charge transfer properties compared to the other materials [9]. Additionally, AUPN possesses plentiful mesopores, which can provide abundant transport channels, shorten the ion diffusion path and reduce charge transfer resistance, thus resulting in the enhanced conductivity and the lowest charge transfer resistance [69]. The equivalent series resistance is shown by the first intersection point of the Nyquist plots on the real axis (ESR). The ESR comprises three components: the ionic resistance of the KOH electrolyte, the intrinsic resistance of the electrode material and the contact resistance at the current collector-active material interface [8,45,52].

The doped samples, particularly AUPN, have comparatively low ESR, which may be attributed to the nitrogen doping's good surface wetting ability. This results in a decreased ESR, suggesting improved electrode conductivity. Because the electrolyte was the same for all electrode materials during the electrochemical investigation, the ionic resistance of the KOH electrolyte should be constant. The difference in ESR is most likely due to the varying resistances of the various carbon electrode materials [11,27]. Furthermore, a cyclic stability test at 4 A/g was carried out to assess how stable the electrode materials are during continual charge–discharge cycles, as shown in Fig. 9 (c). After 1000 cycles, 99%, 97%, 93%, and 84% of specific capacitance were preserved for AUPN, ARPN, ARPP, and AUPP, respectively, indicating high cycling stability. Because of its vast, accessible active sites for ion interaction and partly graphitic nature of carbon, AUPN has the superior capacitance retention [55,70].

The following reasons contribute to AUPN's superior capacitive performance over other capacitors:

1. The high specific area coupled with the large pore volume provides more electrolyte active sites, improving charge storage density.
2. Nitrogen doping improved wettability and electrical conductivity while simultaneously introducing pseudocapacitance.
3. The increased mesopore ratio for AUPN enhances electrolyte ion transport in the porous structure at high current densities

The electrochemical performance of the synthesized hierarchical porous carbons is compared to that of other biomass-derived porous carbons in Table 2.

4. Conclusion

Hierarchical porous carbons were successfully synthesized from plantain peels using a non-toxic molten salt combination of KCl/NaCl as activation medium and NH_4Cl as nitrogen source. The activation was carried out at 800 °C in an air environment. Using a non-toxic mol-

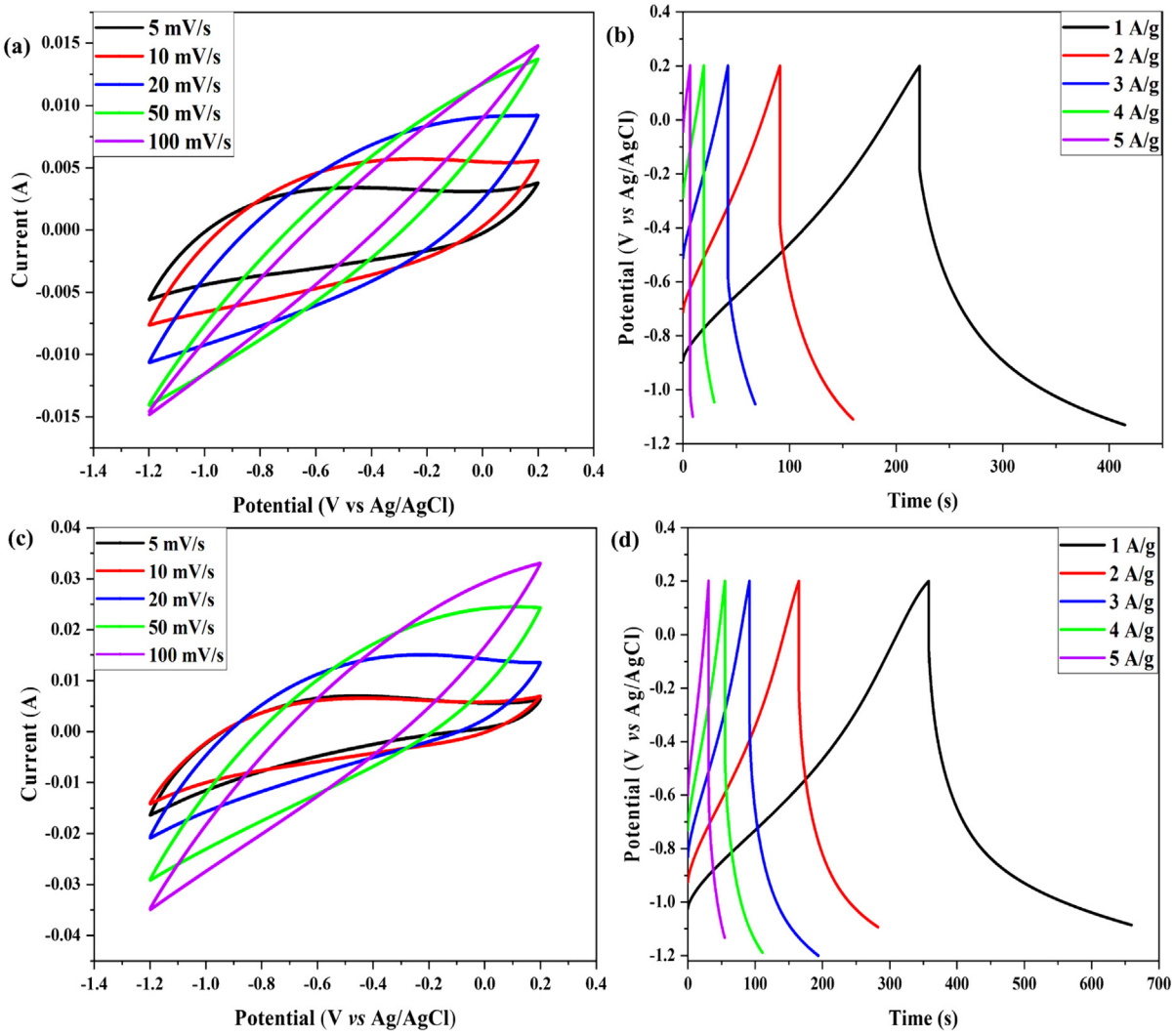

Fig. 8. CV curves at different scan rates and GCD curves at different current densities of ARPP (a,b), CV curves at different scan rates and GCD curves at different current densities of ARPN (c,d).

ten salt mixture in an air atmosphere is more convenient and cost-effective than traditional strategies of synthesizing porous carbon that require the usage of toxic chemicals such as KOH and $ZnCl_2$ and an inert atmosphere, making the whole process expensive and environmentally unfriendly. The obtained hierarchical porous carbons, particularly AUPN, possess excellent properties such, as a thin interconnected porous structure that allows for rapid ion mobility, an efficient double layer for adequate charge storage, high diffusion rates, and nitrogen doping that improves the electrochemical properties by enhancing the wettability of the carbon surface and creating defect sites for charge storage. At 1 A/g, AUPN has the maximum specific capacitance of 550.43 F/g when measured using a three-electrode setup. Also, after 10,000 cycles at 4 A/g, AUPN still had the highest capacitance retention of 99%. This demonstrates its high-rate capabilities and cyclic stability.

These findings also demonstrate that this green and scalable process has the potential to produce porous carbon materials for a wide range of applications.

CRediT authorship contribution statement

Nashiru Mahadeen Nanzumani: Conceptualization, Methodology, Validation, Formal analysis, Resources, Writing – original draft. **Frank Ofori Agyemang:** Conceptualization, Validation, Resources, Supervision, Funding acquisition, Writing – review & editing. **Kwadwo Mensah-Darkwa:** Conceptualization, Validation, Supervision, Writing – review & editing. **Eugene Sefa Appiah:** Conceptualization, Methodology. **Emmanuel Kwesi Arthur:** Writing – review & editing. **Emmanuel Gikunoo:** Writing – review & editing. **Bennetta Koomson:** Writing – review & editing. **Amol R. Jadhav:** Formal analysis. **Akeem Raji:** Writing – review & editing.

Data availability

No data was used for the research described in the article.

Declaration of Competing Interest

The authors declare that they have no known competing financial interests or personal relationships that could have appeared to influence the work reported in this paper.

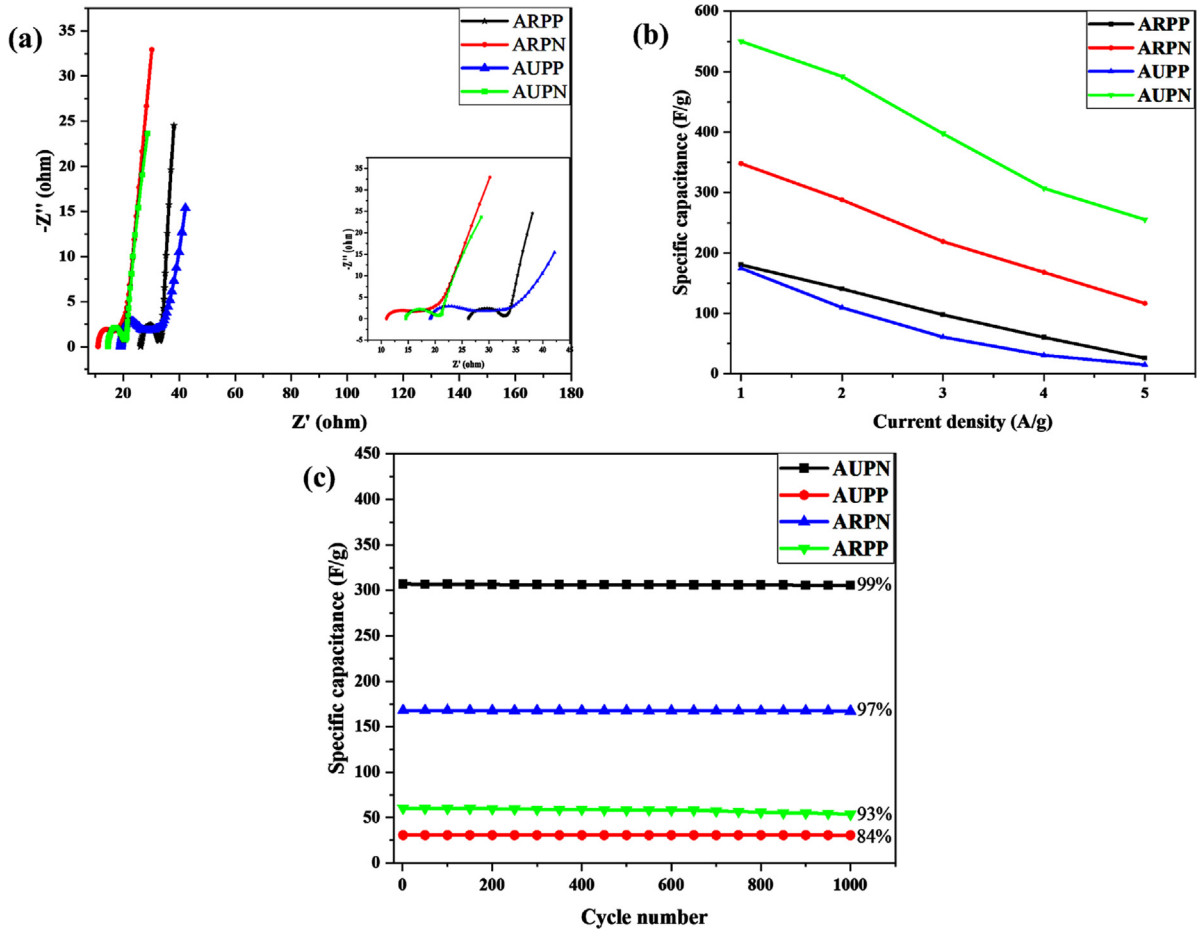

Fig. 9. Nyquist plots for AUPN, ARPN, ARPP, and AUPP in a three-electrode system (a), specific capacitance at various current densities (b) and up to 1,000 cycles of cyclic stability at 4 A/g (c).

Table 2
The electrochemical performance of the synthesized hierarchical porous carbon compared to that of other biomass-derived porous carbons.

Carbon precursor	Activation agent	Heteroatom	Specific capacitance (F/g)	Cell setup	Electrolyte	Ref
Cornstalk	NaCl/KCl	O	407 (1 A/g)	3 electrodes	1 M H_2SO_4	[10]
Cashmere	KOH	N, O	460 (0.5 A/g)	3 electrodes	1 M H_2SO_4	[44]
Rose multiflora	KOH	N, O	340 (0.5 A/g)	3 electrodes	6 M KOH	[71]
Human hair	KOH	N, O, S	999 (1 A/g)	3 electrodes	6 M KOH	[13]
Graphite			271 (2.5 A/g)	3 electrodes	0.1 M KOH	[69]
Starch	$KHCO_3$	O	55.8 (0.5 A/g)	2 electrodes	6 M KOH	[30]
Wool fibre	LiCl/KCl/KNO_3	N	318.2 (0.25 A/g)	3 electrodes	6 M KOH	[12]
Kitchen waste residue	NaCl/KCl	N, O, S	142 (0.2 A/g)	2 electrodes	2 M KOH	[19]
Coal tar pitch	K_2CO_3-KCl	N, O	309.5 (0.25 A/g)	3 electrodes	6 M KOH	[29]
Human hair	KOH	N, O, S	491 (1 A/g)	2 electrodes	egg white gel/1 M NaCl	[21]
Plantain peels	NaCl/KCl	N, O	550 (1 A/g)	3 electrodes	6 M KOH	This work

Acknowledgement

The KEEP CoE Innovation Fund, College of Engineering, Kwame Nkrumah University of Science and Technology, Kumasi, Ghana, provided financial support for this work.

Appendix A. Supplementary data

Supplementary data to this article can be found online at https://doi.org/10.1016/j.jelechem.2022.116645.

References

[1] C. Wang, D. Wu, H. Wang, Z. Gao, F. Xu, K. Jiang, Nitrogen-doped two-dimensional porous carbon sheets derived from clover biomass for high performance supercapacitors, J. Power Sources 363 (2017) 375–383, https://doi.org/10.1016/j.jpowsour.2017.07.097.
[2] X. Lu et al, Molten-salt strategy for fabrication of hierarchical porous N-doped carbon nanosheets towards high-performance supercapacitors, Mater. Chem. Phys. 230 (May 2019) 178–186, https://doi.org/10.1016/j.matchemphys.2019.03.051.
[3] K. Charoensook et al, Preparation of porous nitrogen-doped activated carbon derived from rice straw for high-performance supercapacitor application, J. Taiwan Inst. Chem. Eng. 120 (Mar. 2021) 246–256, https://doi.org/10.1016/j.jtice.2021.02.021.
[4] H. Feng et al, Hierarchical structured carbon derived from bagasse wastes: A simple and efficient synthesis route and its improved electrochemical properties

for high-performance supercapacitors, J. Power Sources 302 (Jan. 2016) 164–173, https://doi.org/10.1016/j.jpowsour.2015.10.063.
[5] E. Bassey, L. Yang, M. Cao, Y. Feng, J. Yao, Molten salt synthesis of capacitive porous carbon from Allium cepa (onion) for supercapacitor application, J. Electroanal. Chem. 881 (Jan. 2021), https://doi.org/10.1016/j.jelechem.2020.114972.
[6] M. Maharjan et al, High surface area bio-waste based carbon as a superior electrode for vanadium redox flow battery, J. Power Sources 362 (2017) 50–56, https://doi.org/10.1016/j.jpowsour.2017.07.020.
[7] N. Díez, A. B. Fuertes, and M. Sevilla, "Molten salt strategies towards carbon materials for energy storage and conversion," *Energy Storage Materials*, vol. 38. Elsevier B.V., pp. 50–69, Jun. 01, 2021, doi: 10.1016/j.ensm.2021.02.048.
[8] J.W. Jeon et al, In situ one-step synthesis of hierarchical nitrogen-doped porous carbon for high-performance supercapacitors, ACS Appl. Mater. Interfaces 6 (10) (May 2014) 7214–7222, https://doi.org/10.1021/am500339x.
[9] J. Cherusseri, K.K. Kar, Hierarchically mesoporous carbon nanopetal based electrodes for flexible supercapacitors with super-long cyclic stability, J. Mater. Chem. A 3 (43) (2015) 21586–21598, https://doi.org/10.1039/c5ta05603a.
[10] C. Wang, D. Wu, H. Wang, Z. Gao, F. Xu, K. Jiang, A green and scalable route to yield porous carbon sheets from biomass for supercapacitors with high capacity, J. Mater. Chem. A 6 (3) (2018) 1244–1254, https://doi.org/10.1039/c7ta07579k.
[11] H. Tan, J. Liu, G. Huang, Y.X. Qian, Y. Deng, G. Chen, Understanding the Roles of Sulfur Doping for Enhancing of Hydrophilicity and Electrochemical Performance of N, S-Codoped Hierarchically Porous Carbon, ACS Appl. Energy Mater. 1 (10) (Oct. 2018) 5599–5608, https://doi.org/10.1021/acsaem.8b01131.
[12] D. Zeng et al, Wool fiber-derived nitrogen-doped porous carbon prepared from molten salt carbonization method for supercapacitor application, J. Mater. Sci. 53 (11) (Jun. 2018) 8372–8384, https://doi.org/10.1007/s10853-018-2035-8.
[13] P. Sinha et al, Keratin-derived functional carbon with superior charge storage and transport for high-performance supercapacitors, Carbon N. Y. 168 (Oct. 2020) 419–438, https://doi.org/10.1016/j.carbon.2020.07.007.
[14] F. Ran, X. Yang, X. Xu, S. Li, Y. Liu, L. Shao, Green activation of sustainable resources to synthesize nitrogen-doped oxygen-riched porous carbon nanosheets towards high-performance supercapacitor, Chem. Eng. J. 412 (May 2021), https://doi.org/10.1016/j.cej.2021.128673.
[15] F. Wu et al, Hierarchical porous carbon microrods derived from albizia flowers for high performance supercapacitors, Carbon N. Y. 147 (Jun. 2019) 242–251, https://doi.org/10.1016/j.carbon.2019.02.072.
[16] A. Gopalakrishnan, T.D. Raju, S. Badhulika, Green synthesis of nitrogen, sulfur-co-doped worm-like hierarchical porous carbon derived from ginger for outstanding supercapacitor performance, Carbon N. Y. 168 (2020) 209–219, https://doi.org/10.1016/j.carbon.2020.07.017.
[17] W. Liu, J. Mei, G. Liu, Q. Kou, T. Yi, S. Xiao, Nitrogen-Doped Hierarchical Porous Carbon from Wheat Straw for Supercapacitors, ACS Sustain. Chem. Eng. 6 (9) (Sep. 2018) 11595–11605, https://doi.org/10.1021/acssuschemeng.8b01798.
[18] S. Liu et al, Nitrogen-doped porous carbons from lotus leaf for CO2 capture and supercapacitor electrodes, Energy and Fuels 33 (7) (Jul. 2019) 6568–6576, https://doi.org/10.1021/acs.energyfuels.9b00886.
[19] P. Li et al, Molten salt and air induced nitrogen-containing graphitic hierarchical porous biocarbon nanosheets derived from kitchen waste hydrolysis residue for energy storage, J. Power Sources 439 (Nov. 2019), https://doi.org/10.1016/j.jpowsour.2019.227096.
[20] B. Lu, L. Hu, H. Yin, X. Mao, W. Xiao, D. Wang, Preparation and application of capacitive carbon from bamboo shells by one step molten carbonates carbonization, Int. J. Hydrogen Energy 41 (41) (Nov. 2016) 18713–18720, https://doi.org/10.1016/j.ijhydene.2016.05.083.
[21] K.D. Verma, P. Sinha, M.K. Ghorai, K.K. Kar, Mesoporous electrode from human hair and bio-based gel polymer electrolyte for high-performance supercapacitor, Diam. Relat. Mater. 123 (Mar. 2022), https://doi.org/10.1016/j.diamond.2022.108879.
[22] P. Tian et al, 'Frying' milk powder by molten salt to prepare nitrogen-doped hierarchical porous carbon for high performance supercapacitor, J. Alloys Compd. 806 (Oct. 2019) 650–659, https://doi.org/10.1016/j.jallcom.2019.07.266.
[23] O.A. Falowo, B. Oladipo, A.E. Taiwo, A.T. Olaiya, O.O. Oyekola, E. Betiku, Green heterogeneous base catalyst from ripe and unripe plantain peels mixture for the transesterification of waste cooking oil, Chem. Eng. J. Adv. 10 (May 2022), https://doi.org/10.1016/j.ceja.2022.100293 100293.
[24] E.E. Imade, T.O. Ajiboye, A.E. Fadiji, D.C. Onwudiwe, O.O. Babalola, Green synthesis of zinc oxide nanoparticles using plantain peel extracts and the evaluation of their antibacterial activity, Sci. African 16 (Jul. 2022), https://doi.org/10.1016/j.sciaf.2022.e01152 e01152.
[25] Z.N. Garba, N.I. Ugbaga, A.K. Abdullahi, Evaluation of optimum adsorption conditions for Ni (II) and Cd (II) removal from aqueous solution by modified plantain peels (MPP), Beni-Suef Univ. J. Basic Appl. Sci. 5 (2) (Jun. 2016) 170–179, https://doi.org/10.1016/j.bjbas.2016.03.001.
[26] E.A. Olatundun, O.O. Borokini, E. Betiku, Cocoa pod husk-plantain peel blend as a novel green heterogeneous catalyst for renewable and sustainable honne oil biodiesel synthesis: A case of biowastes-to-wealth, Renew. Energy 166 (Apr. 2020) 163–175, https://doi.org/10.1016/j.renene.2020.11.131.
[27] J. Cherusseri, K.K. Kar, Ultra-flexible fibrous supercapacitors with carbon nanotube/polypyrrole brush-like electrodes, J. Mater. Chem. A 4 (25) (2016) 9910–9922, https://doi.org/10.1039/c6ta02690g.
[28] R. Samantray et al, A facile approach to fabricate: Saccharum spontaneum -derived porous carbon-based supercapacitors for excellent energy storage performance in redox active electrolytes, Sustain. Energy Fuels 5 (2) (Jan. 2021) 518–531, https://doi.org/10.1039/d0se01420f.
[29] P. Ren, D. Wu, T. Wang, P. Zeng, D. Jia, K2CO3-KCl acts as a molten salt flame retardant to prepare N and O doped honeycomb-like carbon in air for supercapacitors, J. Power Sources 532 (Jun. 2022), https://doi.org/10.1016/j.jpowsour.2022.231072 231072.
[30] J. Zhang, Z. Chen, G. Wang, L. Hou, C. Yuan, Eco-friendly and scalable synthesis of micro-/mesoporous carbon sub-microspheres as competitive electrodes for supercapacitors and sodium-ion batteries, Appl. Surf. Sci. 533 (Dec. 2020), https://doi.org/10.1016/j.apsusc.2020.147511.
[31] X.Q. Zhang, W.C. Li, A.H. Lu, Designed porous carbon materials for efficient CO2 adsorption and separation, Xinxing Tan Cailiao/New Carbon Mater. 30 (6) (Dec. 2015) 481–501, https://doi.org/10.1016/S1872-5805(15)60203-7.
[32] Z. Guo et al, Heteroatom-doped hierarchical porous carbon via molten-salt method for supercapacitors, Electrochim. Acta 360 (Nov. 2020), https://doi.org/10.1016/j.electacta.2020.137022.
[33] R. Chandrabhan Shende, M. Muruganathan, H. Mizuta, M. Akabori, and R. Sundara, "Chemical Simultaneous Synthesis Strategy of Two Nitrogen-Rich Carbon Nanomaterials for All-Solid-State Symmetric Supercapacitor," ACS Omega, vol. 3, no. 12, pp. 17276–17286, Dec. 2018, doi: 10.1021/acsomega.8b02835.
[34] C. Zhang et al, Synthesis of millimeter-sized porous carbon spheres derived from different precursors for CO2 capture, J. Porous Mater. 28 (1) (Feb. 2021) 81–91, https://doi.org/10.1007/s10934-020-00967-0.
[35] C. Peng, J. Lang, S. Xu, X. Wang, Oxygen-enriched activated carbons from pomelo peel in high energy density supercapacitors, RSC Adv. 4 (97) (2014) 54662–54667, https://doi.org/10.1039/c4ra09395j.
[36] J. Cherusseri, R. Sharma, K.K. Kar, Helically coiled carbon nanotube electrodes for flexible supercapacitors, Carbon N. Y. 105 (Aug. 2016) 113–125, https://doi.org/10.1016/j.carbon.2016.04.019.
[37] J. Wang et al, Preparation and application of biomass-based porous carbon with S, N, Zn, and Fe heteroatoms loading for use in supercapacitors, Biomass and Bioenergy 156 (Jan. 2022), https://doi.org/10.1016/j.biombioe.2021.106301.
[38] Y. Tan, Z. Xu, L. He, H. Li, Three-dimensional high graphitic porous biomass carbon from dandelion flower activated by K2FeO4 for supercapacitor electrode, J. Energy Storage 52 (Aug. 2022), https://doi.org/10.1016/j.est.2022.104889 104889.
[39] S. Lu et al, Nitrogen- and oxygen-doped carbon with abundant micropores derived from biomass waste for all-solid-state flexible supercapacitors, J. Colloid Interface Sci. 610 (Mar. 2022) 1088–1099, https://doi.org/10.1016/j.jcis.2021.11.164.
[40] K. Qu et al, Biomass-derived carbon dots regulating nickel cobalt layered double hydroxide from 2D nanosheets to 3D flower-like spheres as electrodes for enhanced asymmetric supercapacitors, J. Colloid Interface Sci. 616 (Jun. 2022) 584–594, https://doi.org/10.1016/j.jcis.2022.02.110.
[41] D. Meng et al, One-step carbonization strategy of freeze-dried chitosan to prepare Nitrogen-Oxygen co-doped porous carbon supercapacitors with ultra-large specific surface area, Fuel 320 (Jul. 2022), https://doi.org/10.1016/j.fuel.2022.124002 124002.
[42] M. Jalalah et al, Novel porous heteroatom-doped biomass activated carbon nanoflakes for efficient solid-state symmetric supercapacitor devices, J. Taiwan Inst. Chem. Eng. 132 (Mar. 2022), https://doi.org/10.1016/j.jtice.2021.11.015.
[43] G. Hu et al, Nitrogen-enriched hierarchical porous carbons derived from biomass waste-discarded pear for ultra-high energy density supercapacitor in neutral aqueous electrolyte, Diam. Relat. Mater. 121 (Jan. 2022), https://doi.org/10.1016/j.diamond.2021.108728.
[44] L. Zhou, H. Cao, S. Zhu, L. Hou, C. Yuan, Hierarchical micro-/mesoporous N- and O-enriched carbon derived from disposable cashmere: A competitive cost-effective material for high-performance electrochemical capacitors, Green Chem. 17 (4) (Apr. 2015) 2373–2382, https://doi.org/10.1039/c4gc02032d.
[45] J. Shao et al, In-situ MgO (CaCO3) templating coupled with KOH activation strategy for high yield preparation of various porous carbons as supercapacitor electrode materials, Chem. Eng. J. 321 (2017) 301–313, https://doi.org/10.1016/j.cej.2017.03.092.
[46] S. Yan et al, Preparation of nitrogen-doped porous carbons for high-performance supercapacitor using biomass of waste lotus stems, RSC Adv. 8 (13) (2018) 6806–6813, https://doi.org/10.1039/c7ra13013a.
[47] O.W. Achaw, G. Afrane, The evolution of the pore structure of coconut shells during the preparation of coconut shell-based activated carbons, Microporous Mesoporous Mater. 112 (1–3) (Jul. 2008) 284–290, https://doi.org/10.1016/j.micromeso.2007.10.001.
[48] L. Sun et al, Isolated boron and nitrogen sites on porous graphitic carbon synthesized from nitrogen-containing chitosan for supercapacitors, ChemSusChem 7 (6) (2014) 1637–1646, https://doi.org/10.1002/cssc.201400048.
[49] Q. Li et al, N, S self-doped porous carbon with enlarged interlayer distance as anode for high performance sodium ion batteries, Int. J. Energy Res. 45 (5) (Apr. 2021) 7082–7092, https://doi.org/10.1002/er.6294.
[50] G. Zhao, Y. Li, G. Zhu, J. Shi, T. Lu, L. Pan, Biomass-based N, P, and S self-doped porous carbon for high-performance supercapacitors, ACS Sustain. Chem. Eng. 7 (14) (Jul. 2019) 12052–12060, https://doi.org/10.1021/acssuschemeng.9b00725.
[51] K. Subhani et al, Porous carbon sponges from collagen-rich biomass waste for high-performance supercapacitors, Mater. Today Sustain. 18 (Jun. 2022), https://doi.org/10.1016/j.mtsust.2022.100152 100152.
[52] Z. Sun et al, Unveiling intrinsic potassium storage behaviors of hierarchical Nano Bi@N-doped carbon nanocages framework via in situ characterizations, Angew. Chemie - Int. Ed. 60 (13) (Mar. 2021) 7180–7187, https://doi.org/10.1002/anie.202016082.
[53] Y.K. Penke, P. Sinha, A.K. Yadav, J. Ramkumar, K.K. Kar, Al3+-doped 3d-transitional metal (Mn/Cu) ferrite impregnated rGO for PEC water-

splitting/supercapacitor electrode with oxygen vacancies and surface intercalation aspects, Compos. Part B Eng. 202 (Dec. 2020), https://doi.org/10.1016/j.compositesb.2020.108431.
[54] W. Luo et al, Pyrolysis of cellulose under ammonia leads to nitrogen-doped nanoporous carbon generated through methane formation, Nano Lett. 14 (4) (Apr. 2014) 2225–2229, https://doi.org/10.1021/nl500859p.
[55] Q. Bai, H. Li, L. Zhang, C. Li, Y. Shen, H. Uyama, Flexible solid-state supercapacitors derived from biomass konjac/polyacrylonitrile-based nitrogen-doped porous carbon, ACS Appl. Mater. Interfaces 12 (50) (Dec. 2020) 55913–55925, https://doi.org/10.1021/acsami.0c16752.
[56] K. Thileep Kumar *et* al., Synthesis of nanoporous carbon with new activating agent for high-performance supercapacitor, Mater. Lett., 218, 181–184, May 2018, doi: 10.1016/j.matlet.2018.02.017.
[57] B. Saravanakumar, K.K. Purushothaman, G. Muralidharan, Fabrication of two-dimensional reduced graphene oxide supported V2O5 networks and their application in supercapacitors, Mater. Chem. Phys. 170 (Feb. 2016) 266–275, https://doi.org/10.1016/j.matchemphys.2015.12.051.
[58] Y. Cheng et al, Molten salt synthesis of nitrogen and oxygen enriched hierarchically porous carbons derived from biomass via rapid microwave carbonization for high voltage supercapacitors, Appl. Surf. Sci. 439 (May 2018) 712–723, https://doi.org/10.1016/j.apsusc.2018.01.006.
[59] B. Chang, H. Yin, X. Zhang, S. Zhang, B. Yang, Chemical blowing strategy synthesis of nitrogen-rich porous graphitized carbon nanosheets: Morphology, pore structure and supercapacitor application, Chem. Eng. J. 312 (2017) 191–203, https://doi.org/10.1016/j.cej.2016.11.129.
[60] C. Chang, M. Li, P. Niu, L. Zhang, S. Wang, A facile dual-functional hydrothermal-assisted synthesis strategy of hierarchical porous carbon for enhanced supercapacitor performance, Sustain. Mater. Technol. 28 (Jul. 2021), https://doi.org/10.1016/j.susmat.2021.e00265.
[61] J. Zhang *et al.*, "Electronic Supplementary Information (ESI) Green self-activation engineering of metal-organic frameworks derived hollow nitrogen-doped carbon spheres towards supercapacitors," 2021.
[62] T. Chen et al, High energy density supercapacitors with hierarchical nitrogen-doped porous carbon as active material obtained from bio-waste, Renew. Energy 175 (Sep. 2021) 760–769, https://doi.org/10.1016/j.renene.2021.05.006.
[63] Y.K. Penke, A.K. Yadav, P. Sinha, I. Malik, J. Ramkumar, K.K. Kar, Arsenic remediation onto redox and photo-catalytic/electrocatalytic Mn-Al-Fe impregnated rGO: Sustainable aspects of sludge as supercapacitor, Chem. Eng. J. 390 (Jun. 2020), https://doi.org/10.1016/j.cej.2019.124000.
[64] Y. Hao, F. Xu, M. Qian, J. Xu, W. Zhao, F. Huang, Low-cost and massive preparation of nitrogen-doped porous carbon for supercapacitor application, RSC Adv. 7 (18) (2017) 10901–10905, https://doi.org/10.1039/c6ra28354c.
[65] C. Wang, X. Yuan, L. Luo, Z. Ma, P. Li, Y. Miao, Salt shielded preparation of MOF-derived open hollow carbon structure in air for high-performance supercapacitors, J. Alloys Compd. 900 (Apr. 2022), https://doi.org/10.1016/j.jallcom.2021.163330.
[66] L. Hou et al, Dual-template endowing N, O co-doped hierarchically porous carbon from potassium citrate with high capacitance and rate capability for supercapacitors, Chem. Eng. J. 417 (Aug. 2021), https://doi.org/10.1016/j.cej.2021.129289.
[67] Y. Chen, K. Cai, C. Liu, H. Song, X. Yang, High-performance and breathable polypyrrole coated air-laid paper for flexible all-solid-state supercapacitors, Adv. Energy Mater. 7 (21) (2017) Nov, https://doi.org/10.1002/aenm.201701247.
[68] J. Cherusseri, K.K. Kar, Polypyrrole-decorated 2D carbon nanosheet electrodes for supercapacitors with high areal capacitance, RSC Adv. 6 (65) (2016) 60454–60466, https://doi.org/10.1039/c6ra01402j.
[69] R. Kumar, S. Sahoo, W.K. Tan, G. Kawamura, A. Matsuda, K.K. Kar, Microwave-assisted thin reduced graphene oxide-cobalt oxide nanoparticles as hybrids for electrode materials in supercapacitor, J. Energy Storage 40 (Aug. 2021), https://doi.org/10.1016/j.est.2021.102724.
[70] L. Wan, J. Wang, L. Xie, Y. Sun, K. Li, Nitrogen-enriched hierarchically porous carbons prepared from polybenzoxazine for high-performance supercapacitors, ACS Appl. Mater. Interfaces 6 (17) (Sep. 2014) 15583–15596, https://doi.org/10.1021/am504564q.
[71] Q. Chen et al, Sustainable rose multiflora derived nitrogen/oxygen-enriched micro-/mesoporous carbon as a low-cost competitive electrode towards high-performance electrochemical supercapacitors, RSC Adv. 8 (17) (2018) 9181–9191, https://doi.org/10.1039/c8ra00858b.